Journal of Volcanology and Geothermal Research 433 (2023) 107727

Contents lists available at ScienceDirect

Journal of Volcanology and Geothermal Research

journal homepage: www.journals.elsevier.com/journal-of-volcanology-and-geothermal-research

The effect of weak Mohr–Coulomb layers on the onset of caldera collapse - A limit analysis modelling approach

Elisabeth Hoffstad Reutz [a,b], Olivier Galland [a,*]

[a] The Njord Centre, Depatment of Geosciences, University of Oslo, P.O. box 1047 Blindern, 0316 Oslo, Norway
[b] Now at Norwegian Geotechnical Institute, Postboks 3930 Ullevål Stadion, 0806 Oslo, Norway

ARTICLE INFO

Keywords:
Caldera collapse
Mohr–Coulomb layering
Limit analysis
Caldera fault
Plasticity

ABSTRACT

Calderas are subcircular volcanic depressions that can occur due to drainage of a subsurface magma reservoir. Numerous models simulating the initiation and growth of caldera collapse consider homogeneous overburden of the magma reservoir. This study describes plastic models implementing limit analysis to investigate the effects of weak layers (low cohesion and low friction) on caldera formation and structure. Our models show that the presence of weak layers within the crust favours the onset of caldera collapse, as it reduces the critical magma underpressure within the magma chamber to initiate roof failure. This effect is more pronounced with greater cumulated thickness of weak layers. In homogeneous models, the onset of caldera collapse is accommodated by a simple, localized outward dipping reverse damage band (caldera fault), whereas in layered models caldera collapse is accommodated by more complex damage structures. Weak layers confine damage underneath the layers, limiting the growth of the caldera fault toward the surface. Calculated stress trajectories are rotated across weak layers, showing that weak layers act as stress barriers. The effect of weak layers is stronger when the layer is closer to the magma reservoir, where layer-parallel damage form underneath the layer, interpreted as a potential detachment level. Multiple layers trigger more distribution of the damage and several layer-parallel damage bands. The subsurface distribution of damage due to weak layers may lead to more distributed surface subsidence, enhancing sagging before a caldera fault reaches the surface. Finally, internal detachments due to weak layers are likely important for observed episodic transient subsurface collapse episodes before collapse occurs at surface. All in all, our models that implement plastic deformation predict significant stress perturbations as a result of varying Mohr–Coulomb properties only. Our study thus shows that widely used static elastic models are not sufficient for physically relevant stress analyses of geological systems. In addition, our study shows that plastic (or elasto-plastic) models are necessary to predict the location and extent of inelastic damage accommodating volcano deformation and failure.

1. Introduction

Calderas are subcircular volcanic depressions that occur in different tectonic (extensional, compressional, strike-slip or neutral) and magmatic (felsic to mafic) settings, both on Earth and other planets in the solar system (Cole et al., 2005; Acocella, 2007; Martí et al., 2008). Calderas result from the drainage of a subsurface magma reservoir. The magma withdrawal can either result from a large volcanic eruption (Druitt and Sparks, 1984; Cole et al., 2005) or subsurface lateral migration of magma (Geshi et al., 2002; Gudmundsson et al., 2016; Anderson et al., 2019; Fontaine et al., 2019). As magma withdraws from the chamber, the roof eventually experiences down-sag due to the loss of support, which may evolve to fault-controlled subsidence (Lipman, 1997; Roche et al., 2000; Acocella, 2007; Liu et al., 2019).

Numerous models simulating the initiation and growth of caldera collapse consider homogeneous overburden of the draining magma reservoir (Roche et al., 2000; Roche and Druitt, 2001; Cole et al., 2005; Geyer et al., 2006; Martí et al., 2008; Burchardt et al., 2012; Holohan et al., 2015; Liu et al., 2019). However, the Earth's brittle crust is strongly heterogeneous, as it contains faults, fractures, and layers of different lithologies and mechanical properties. Mechanical layering is shown to have significant impact on geological processes such as tectonic deformation (Rossi and Storti, 2003; Holland et al., 2006; van Gent et al., 2010) and magma emplacement (Thomson and Schofield, 2008;

* Corresponding author.
E-mail address: olivier.galland@geo.uio.no (O. Galland).

https://doi.org/10.1016/j.jvolgeores.2022.107727
Received 4 July 2022; Received in revised form 19 November 2022; Accepted 25 November 2022
Available online 29 November 2022

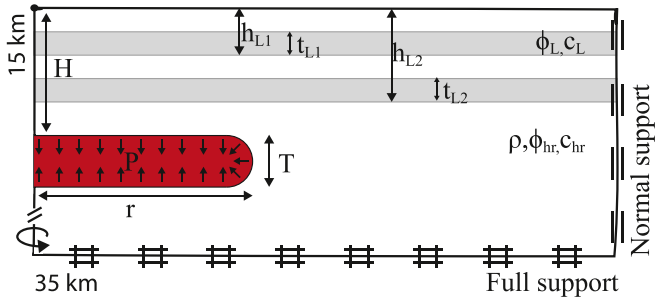

Fig. 1. Sketch of model setup used in OptumG2. The model considers a magma chamber positioned at a constant depth H, with constant thickness T, and varying radius r. The magma chamber exerts a constant pressure P on its walls and is placed within a homogeneous and isotropic Mohr–Coulomb material. Layers of thickness t and depth h, of different cohesion C and friction angle ϕ can be inserted in the overburden of the reservoir. The system is axisymmetric. The boundary conditions are free surface at the top, normal support to the right, and full support at the bottom.

Abdelmalak et al., 2016; Reynolds et al., 2018; Yao et al., 2018; Souche et al., 2019). To which extent mechanical layering of the Earth's crust affects caldera formation and structure remains poorly understood.

Most numerical modelling investigating the conditions of caldera collapse are overall based on static stress analyses (*e.g.,*Long and Grosfils, 2009; Browning and Gudmundsson, 2015a; Gudmundsson, 2020). Some heterogeneities such as faults (Browning and Gudmundsson, 2015a) or layers (Long and Grosfils, 2009) of contrasting elastic stiffness can be implemented. Even though these models predict complex stress perturbations due to heterogeneity, failure is only inferred by comparing calculated stresses with rock strength, such that the damage associated to the caldera faults is not simulated and cannot be investigated. In addition, Souche et al. (2019) show that static stress calculations are not conclusive for inferring the mode and geometry of failure structures, and plastic or elastoplastic models are required (Holohan et al., 2015).

This study describes plastic deformation models implementing limit analysis to investigate the effects of weak layers (low cohesion and low friction) on caldera formation and structure. We show how weak layers affect (1) the critical pressure (P_c) required to initiate failure in the overburden, and (2) the shape of caldera faults and the associated distribution of inelastic damage.

2. Model concept and Setup

We investigate the conditions for plastic deformation leading to failure and the stability of the brittle roof of a magma chamber using the limit analysis software OptumG2, created for geotechnical stability analysis (Krabbenhøft et al., 2016a). This approach has been applied for several geological systems, including fold-and-thrust and thrust belts (Souloumiac et al., 2010; Cubas et al., 2013) and overpressurised sills (Haug et al., 2017; Haug et al., 2018; Schmiedel et al., 2019). The same approach and methods as those of Haug et al. (2018) and Schmiedel et al. (2019), who implemented limit analysis with OptumG2 to look at inelastic deformation connected to overpressured sills, will be used in this study, however, underpressure within the magma chamber will be applied. This scenario is favoured as caldera collapse associated with magma drainage and underpressure is the most common (Geyer and Marti, 2008).

Limit analysis predicts an approximate value of the collapse load, and is based on the lower bound and upper bound theorems, known as the collapse load theorems (*e.g.,*Davis and Selvadurai, 2005). The lower bound theorem is used to find the highest load where failure will not occur, while the upper bound theorem is used to find the lowest load where failure is guaranteed to occur. The true collapse load will therefore be between the two bounds. This implies that the smaller the difference between the lower and upper bounds, the better constrained is the actual critical load that leads to failure (Davis and Selvadurai, 2005; Krabbenhøft et al., 2005; Haug et al., 2018).

Table 1
List of parameters and the range of their values used in this study.

Notation	Parameters	Range of value
H	Overburden thickness [km]	5
T	Thickness of chamber [km]	2
r	Magma chamber radius [km]	2.25–13.5
C_{hr}	Cohesion host rock [kPa]	10000
ϕ_{hr}	Friction angle host rock	30°
ρ	Density [kg/m^3]	2500
h_{Li}	Depth of bottom of weak layer [km]	0.5–4
t_{Li}	Weak layer thickness [km]	0.5–2
C_L	Cohesion layer [kPa]	100
ϕ_L	Friction angle layer	15°
g	Acceleration due to gravity [m/s^2]	9.81
ΔP	Underpressure [kPa]	–

Limit analysis is used in this study to constrain the critical pressure within the magma chamber needed to trigger failure of the overburden of a magma reservoir, *i.e.,* the onset of caldera collapse. OptumG2 creates plots with the shear energy dissipation, which is derived from the deviatoric part of the strain tensor and displays the energy dissipated by shear, allowing us to determine the shape of the fault surface. For commodity the energy shear dissipation will be referred to as damage in this paper.

The model considers a sill-like under-pressurised cavity, representing a magma chamber. We chose a flat-roof sill-like geometry for the magma chamber because it seems to be a good representation of plutons and magma chambers (*e.g.,*Gudmundsson, 2007; Bartley et al., 2012; Burchardt et al., 2012; Gudmundsson, 2012); other chamber geometries could have been implemented but this is beyond the scope of this study. In addition, a flat roof geometry allows simpler definition of the depth of magma reservoirs of variable radius compared to an elliptic geometry, *i.e.*, the depth of the chamber's roof is not variable with varying diameter (Fig. 1). It is located at a depth H, with a radius r and a constant thickness T, within a homogeneous and isotropic Mohr–Coulomb host rock, with a cohesion C_{hr}, an angle of internal friction ϕ_{hr} and a density ρ (Fig. 1).

In the software OptumG2, the numerical domain is 15 km deep, and 35 km wide. The effect of the size of the numerical domain was tested and had a negligible effect as long as the numerical domain is significantly larger than the modelled magma reservoir, showing that boundary conditions have negligible effects on the modelling results. The upper boundary has a free surface, the right boundary prevents normal displacement, and the bottom boundary prevents all slip (Fig. 1). The system is solved in axisymmetric geometry by using adaptive mesh, starting with 5000 elements and ending with 55 000 elements in the final mesh (Krabbenhøft et al., 2016a; Krabbenhøft et al., 2016b). The size of an element in the model (x10 meters) does not allow simulating microscopic rock deformation processes such as pore-scale and grain-scale deformation. The damage simulated by OptumG2 is thus macroscopic at the scale of fault zones.

Our models implement weak layers of varying depth, thickness and number. The density of the weak layers and background rock (subsequently referred to as the host rock) is set to 2500 kg m^{-3}. The cohesion and angle of internal friction of the host rock are 10 MPa and 30°, respectively, while the cohesion and angle of internal friction of the weak layers are set to 0.1 MPa and 15°, respectively (Table 1). Since this is a preliminary study on the potential effects of weak layers, we have chosen very low strength-values (for the cohesion and angle of internal friction) in order to create a large contrast between the host rock and the weak layers. We are aware that these values are extremely too, in particular too low to account for intact rocks, regardless its lithology. However, other processes at active volcanoes can considerably reduce

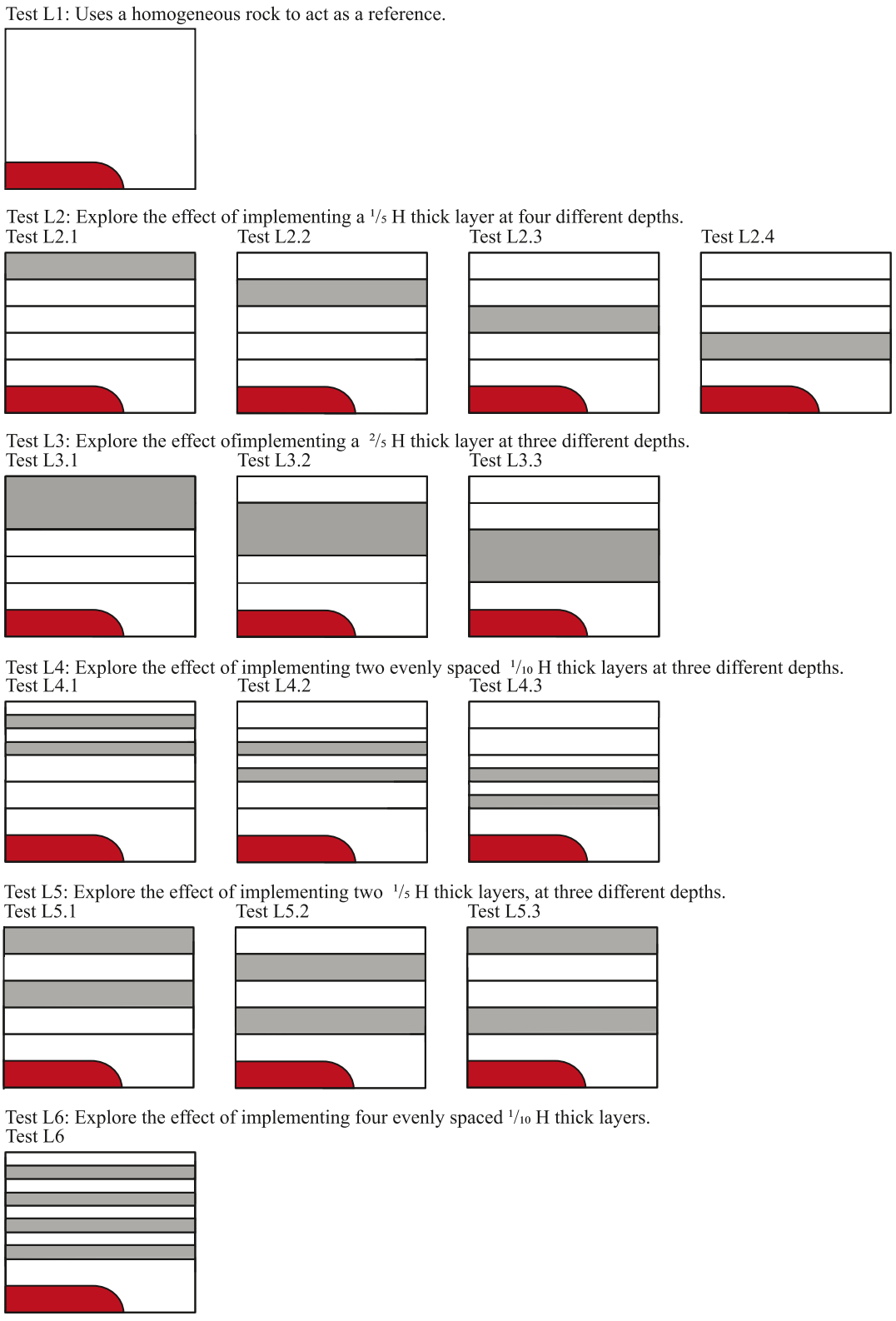

Fig. 2. Sketch displaying the Overview of the layer configurations used for the simulations. The weak layers are coloured grey. Test 1 (top) uses a homogeneous rock. Test 2 (second row) implements one layer at different depth. Test 3 (third row) implements a thick layer than in Test 2 at different depth. Test 4 (fourth layer) implements two separated thin layers; the summed thickness of the layers is equivalent to the thickness of one layer in Test 2. Test 5 (fifth row) implements two separated layers at different configurations. Test 6 (bottom row) implements four separated thin layers; the summed thickness of the layers is equivalent to the thickness of one layer in Test 3. Each test is run for three different $R = 0.19$, 0.71 and 1.1. The figure is only for illustrative purposes and is not to scale.

Table 2
List of model parameters implemented in this study. Each model was run for both upper and lower bound, and for depth-to-diameter aspect ratios $R = 0.19$, $R = 0.71$ and $R = 1.1$.

Exp.	Nr. of layers	Layer thickness [km]	Layer depths [km]
L1	–	–	–
L2.1	1	1	1
L2.2	1	1	2
L2.3	1	1	3
L2.4	1	1	4
L3.1	2	1	1 and 2
L3.2	2	1	2 and 3
L3.3	2	1	3 and 4
L4.1	2	0.5	1 and 2
L4.2	2	0.5	2 and 3
L4.3	2	0.5	3 and 4
L5.1	2	1	1 and 3
L5.2	2	1	2 and 4
L5.3	2	1	1 and 4
L6	4	0.5	1, 2, 3 and 4

rock cohesion and friction, such as rock alteration to clay (*e.g.* talc; Giorgetti et al., 2015) and high fluid pressures (Mourgues and Cobbold, 2003), which are common in hydrothermal systems in volcanoes.

The weak layers are implemented with uniform thickness and depth, and placed with different configurations in the roof of the magma chamber, as seen in Fig. 2. The deepest layer is kept at $\frac{1}{5}H$ distance from the magma chamber, so that it does not interfere with the chamber. The model does not treat the contacts between the layers and the surrounding rock as weak interfaces (see discussion in Kavanagh and Pavier, 2014), such that only the contrasts between the layers affect the results.

Each layer configuration is implemented for three different values of the depth-to-diameter ratio ($R = H/D$) of the magma chamber ($R = 0.19, 0.71$ and 1.1) achieved by changing the radius of the chamber. For clarity and concision of the paper, we will not display all simulations results for all values of R, but we will select the model geometry that displays the most characteristic results. Table 2 lists all the numerical tests performed in this study: we ran a total of 15 tests of different layer configurations. In each layer configuration, we ran models with depth-to-diameter aspect ratios of the reservoir $R = 0.19$, $R = 0.71$ and $R = 1.1$, and calculated both the upper and lower bound (total: 90 models). For each test, the model outcomes are (1) both the upper bound and lower bound of the critical pressure within the magma reservoir needed to initiate failure in the overburden, (2) cross section maps of the shear energy dissipation pattern, subsequently referred to as damage, (3) and for selected tests, cross section maps of stresses used to compute stress trajectories of σ_1 and σ_3.

Limit analysis is designed to address the conditions for initial failure, not to model the evolution of geological structures. Therefore, the models only calculate the damage distribution at the onset of caldera collapse, but does not provide information on the final structure as observed in the field (*e.g.,*Cole et al., 2005; Kennedy et al., 2018) or in laboratory models (*e.g.,*Acocella, 2007; Burchardt and Walter, 2010; Liu et al., 2019). It is possible to implement limit analysis to model the evolution of geological structures (Souloumiac et al., 2010; Cubas et al., 2013), but the implementation requires in-house advanced algorithms that expand beyond the use of OptumG2.

3. Results

The maps displaying damage correspond to the upper bound calculations (see *e.g.,*Fig. 3). The distributed damage indicates areas of plastic deformation and can reveal the location of a fault. In each figure displaying the damage, the colour scale is constant between the plots to emphasise how both the distribution and the intensity of plastic damage is affected by the weak layer configurations. In the areas where the plastic damage is concentrated, it will be referred to as a "damage zone", and when it is not concentrated, the damage will be referred to as "distributed damage". The presented pressure plots display the absolute values of chamber underpressure necessary for fault nucleation, scaled by the confining pressure $\Delta P/\rho gH = (\rho gH - P_c)/\rho gH$, and the resulting values are positive.

3.1. Test L1: homogeneous models

The homogeneous models will be used as reference to highlight the effects of weak layers in the other models. In the three simulations of Test L1 (Fig. 3), the damage is concentrated along a single band, and the intensity of the damage zone is highest at the magma chamber edge and fades towards the surface. We note some differences of the damage zone as a function of the value of R. For $R = 0.19$ the damage zone is curved outward (Fig. 3, left), while for $R = 0.71$ and $R = 1.1$ the damage zone is straight, with a dip range of $\approx 55-70°$ (Fig. 3, centre and right). In addition, in the simulations with $R = 0.19$ and $R = 0.71$, the damage zone reaches the surface (Fig. 3, left and centre), whereas it does not in the simulation with $R = 1.1$ (Fig. 3, right). We notice as well that the damage zone in the simulation with $R = 0.71$ exhibits two branches that are next to each other. Overall, the results of the simulations with $R = 0.71$ and $R = 1.1$ are consistent with former modelling studies of caldera collapse (*e.g.,*Roche et al., 2000; Acocella, 2007; Holohan et al., 2015; Holohan et al., 2017). Conversely, we notice that the curving of the experiment with $R = 0.19$ is reverse to those observed in laboratory models of caldera collapse (*e.g.,*Roche et al., 2000; Acocella, 2007), where the curving is convex, *i.e.* having a bell-shape. Such difference might result from a sensibly lower value of friction angle used in our models (see how damage zone vary with varying angle of friction in the models of Haug et al., 2018).

3.2. Test L2: effect of layer depth

Fig. 4 displays damage maps with a weak layer of thickness $\frac{1}{5}H$ located at variable depth. The left map of Fig. 4 displays Test L1 as the

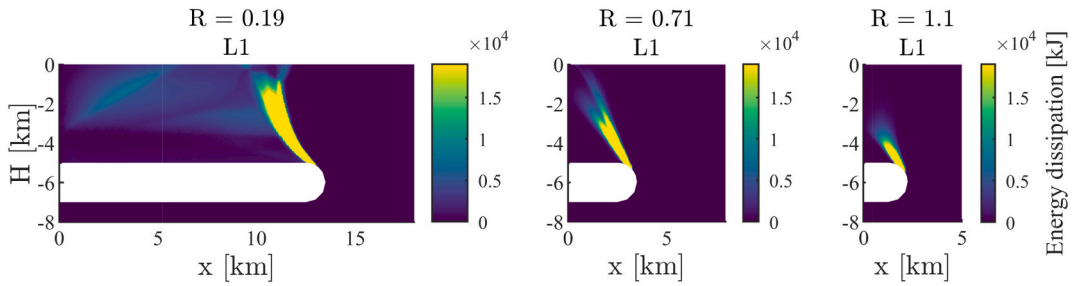

Fig. 3. Cross-section maps of distribution of shear energy dissipation (in kJ) in the overburden of the magma chamber (represented by the horizontal white sill). Figure displays three models with varying R (0.19, 0.71 and 1.1). These simulations are preformed with a homogeneous crust. The energy dissipation localises along a narrow damage zone nucleating at the edge of the magma chamber towards the surface.

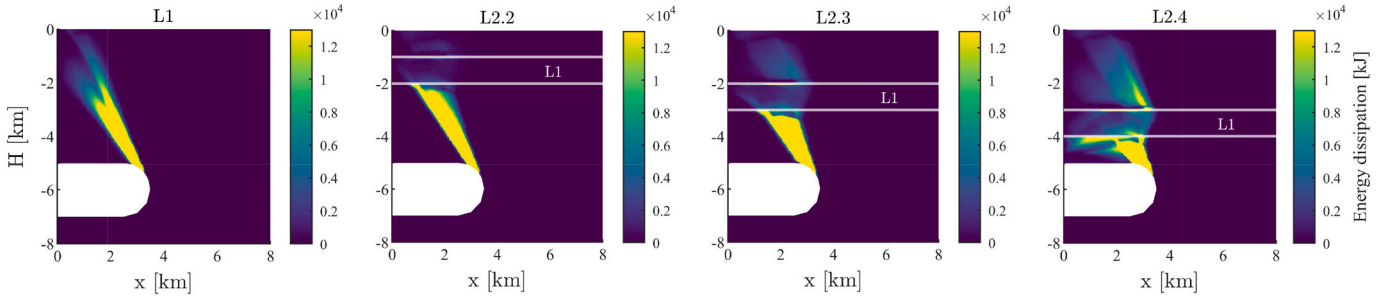

Fig. 4. Cross-section maps of distribution of shear energy dissipation (in kJ) in the overburden of the magma chamber in four simulations (for $R = 0.71$). The left simulation is homogeneous, whereas the three others contain a weak layer of thickness $t = \frac{1}{5}H$, located between white horizontal lines, of variable depth. Depth of bottom of weak layer is $\frac{2}{5}H$ in test L2.2, $\frac{3}{5}H$ in test L2.3 and $\frac{4}{5}H$ in test L2.4.

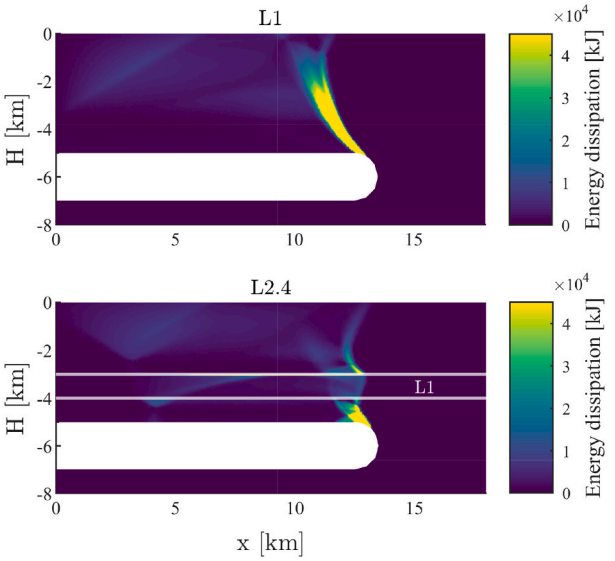

Fig. 5. Cross-section maps of damage distribution in the overburden of the magma chamber (for $R = 0.19$). From one test with a $\frac{1}{5}H$ thick weak layer is positioned $\frac{1}{5}H$ from the magma chamber. The R-value is 0.19. The colourbar represents the plastic shear dissipation (in kJ), and is chosen relative to the maximum value for each simulation.

homogeneous reference.

In Test L2.2 (shallowest layer, layer depth $\frac{2}{5}H$; Fig. 4), the damage zone is localized, almost at the same location as in the homogeneous model. Nevertheless, the damage zone is restricted under the weak layer, and so shorter. In Test L2.3 (layer depth $\frac{3}{5}H$; Fig. 4), most of the damage is also constrained under the layer. However, the damage zone appears wider than in Test L2.2, and some low intensity, distributed damage is visible above the weak layer, and some within the layer. The damage distribution becomes significantly different in Test L2.4 (deepest layer, layer depth $\frac{4}{5}H$; Fig. 4). Intense damage occurs under the layer, along a damage band that nucleates from the tip of the reservoir, and inward along a band just under the weak layer. Damage is also visible through the weak layer. Finally, a weak and somehow distributed damage band also affects the overburden above the weak layer. The band has similar dip angle as in the homogeneous Test L1, but its location is moved further out. Interestingly, the dip angle of the damage within the weak layer is inward-dipping, whereas it is outward-dipping in the host rock below and above.

The change of dip direction of the damage zone through a deep weak layer is even more pronounced in model with $R = 0.19$ (Test L2.4, Fig. 5). Even though the damage zone reaches the surface with very low energy, it can be seen that in this model, the damage zone exhibits a strongly curved shape above the weak layer, leading to a larger diameter of the caldera compared to Test L1. The change in dip direction of the damage zone is likely associated with a change in kinematics, outward-dipping and inward-dipping damage zones being usually associated with reverse and normal faulting, respectively.

Fig. 6 displays the calculated relative critical underpressure within the magma chamber ($\Delta P/\rho gH$) as a function of the depth of the weak layer. The results are given for both the upper (crosses) and lower (open circle) bound solutions. Fig. 6 includes the results for all the values of R. Note that the differences between the lower bound and the upper bound are small. This implies that the estimates of the critical underpressure are robust and well constrained. The difference between the relative underpressure required to trigger failure $\Delta P/\rho gH$ is quite clear for the different values of R. Simulations with $R = 0.19$ require less underpressure within the magma chamber to trigger failure of the overburden, compared to $R = 0.71$ and 1.1 which require larger underpressure within the chamber. This result is in good agreement with former studies of the critical pressure for the onset of caldera collapse (Roche and Druitt, 2001).

The results show that $\Delta P/\rho gH$ are always lower with a weak layer with respect to the homogeneous model. However, the value of $\Delta P/\rho gH$ is similar between the homogeneous model of Test L1 and the Test L2.1 with the shallowest layer. The effect of the layer depth on the critical underpressure is more significant than the presence of a weak layer: the deeper the weak layer, the lower the critical underpressure (Fig. 6). Note that the same trend is observed for the three values of R, however the trend is weaker for $R = 0.19$ (Fig. 6, red). In the following sections, we will only consider the underpressure results for the simulations with $R = 0.71$ and $R = 1.1$.

The results discussed above focus on the simulation series with a weak layer of thickness $\frac{1}{5}H$. The correlations between the varying damage patterns and critical underpressure with the depth of a weak layer are very similar when the layer is thicker ($\frac{2}{5}H$)(compare top row and bottom row of Fig. 7). The qualitative effects of the depth of a weak layer is therefore the same for variable thickness of the layer.

3.3. Effect of layer thickness

Fig. 7 displays damage distribution maps for simulations with variable thickness of the weak layer. In particular, one can compare the results between models with a thick weak layer (t=$\frac{2}{5}H$; top row in Fig. 7) and models with a thinner layer (t=$\frac{1}{5}H$; bottom row in Fig. 7). Between the top and bottom row of Fig. 7, the depth of the bottom of the weak layers is the same. Overall, the effect of the layer depth on the damage distribution is very similar between the thin layer (Section 3.2 and bottom row of Fig. 7) and the thick layer (top row of Fig. 7), *i.e.* the layer tends to confine a damage band underneath.

The first main difference is that the maximum values of the damage is systematically higher (up to 50%, see colour scales in Fig. 7) in the

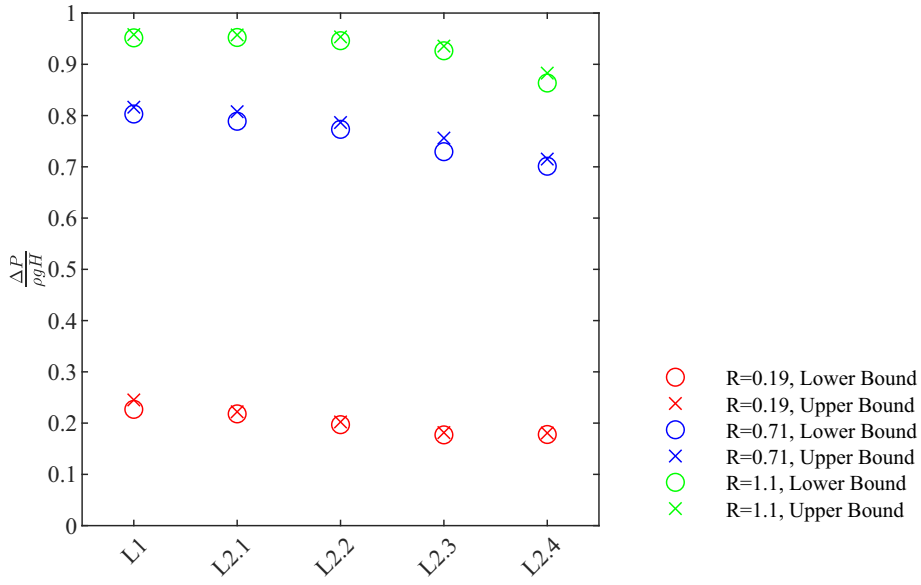

Fig. 6. Plot of the scaled critical underpressure $\frac{\Delta P}{\rho g H}$ in the magma chamber as a function of depth of weak layer of thickness $\frac{1}{5}H$. Circles gives the lower bound solution, while crosses give the upper bound solution. Results are for models with $R = 0.19$ (red), $R = 0.71$ (blue) and $R = 1.1$ (green). Simulations with $R = 0.71$ are those of Fig. 4.

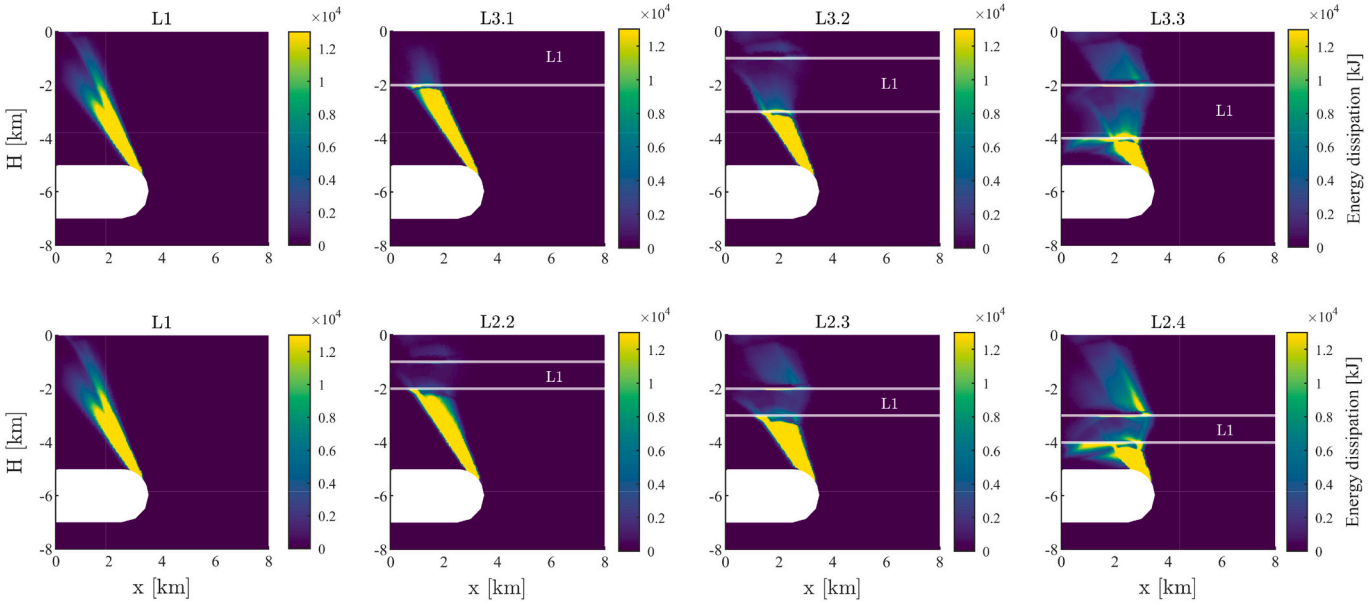

Fig. 7. Cross-section maps of distribution of shear energy dissipation (in kJ) in the overburden of the magma chamber in different simulations (for $R = 0.71$). In both upper and lower row, overburden in left simulation is homogeneous. Three other simulations in top row have a weak layer of thickness $t = \frac{2}{5}H$ (bounded by horizontal white lines) at variable depth. The three other simulations in bottom row have a weak layer of thickness $t = \frac{1}{5}H$ (bounded by horizontal white lines) at variable depth. Depth of bottom of weak layers are the same in both sets of simulations.

models with thick layer than those with a thin layer. This suggests that the damage concentration is more efficient below the thick layer, *i.e.* the thick layer confines even more the damage underneath.

The most noticeable effect of the layer thickness is visible when it is deepest (compare between Tests L2.4 and L3.3 in Fig. 7). The damage map in Test L3.3 shows that the thick layer enhances distributed damage across it, which as a result also leads to more distributed damage above it in comparison to Test L2.4. Notice that for both Tests L2.4 and L3.3, the outer edge of the damage area is inward dipping within the weak layer, whereas it is outward dipping underneath and above the layer. It can also be seen that the thin weak layer in Test L2.4 enhances a concentration of damage under the layer along the interface, which is less the case for Test L3.3.

Fig. 8 shows that $(\Delta P/\rho g H)$ is systematically lower in the thick layer simulations than in the thin layer simulations. This is expected as the overall strength of the reservoir's overburden is lower. However, one can notice that the difference of $(\Delta P/\rho g H)$ between the thick layer and the thin layer models increases with increasing depth of the weak layer. Even though the gap between the lower bound and upper bound increases for increasing depth of the weak layer (Fig. 8), the effect of a thick layer increases with increasing depth.

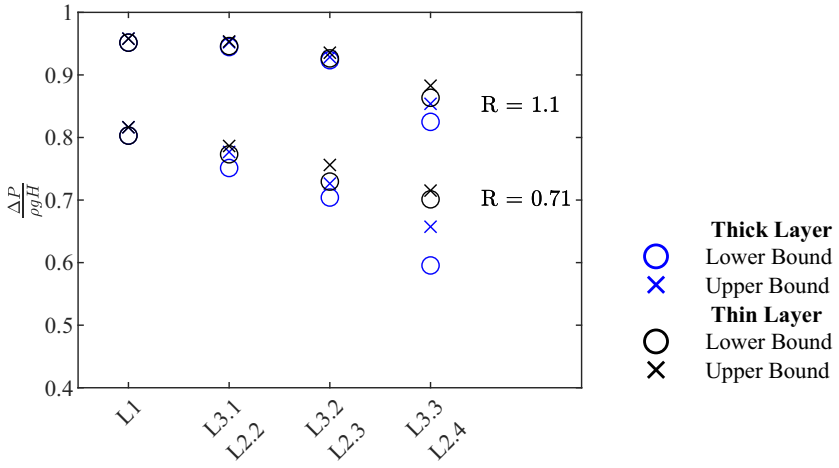

Fig. 8. Plot of the scaled critical underpressure $\frac{\Delta P}{\rho g H}$ in the magma chamber as a function of depth and thickness ($t = \frac{2}{5}H$, black; $t = \frac{2}{5}H$, blue) of weak layer. Circles gives the lower bound solution, while crosses give the upper bound solution. Results are for models with $R = 0.71$ and $R = 1.1$. Simulations with $R = 0.71$ are those of Fig. 7.

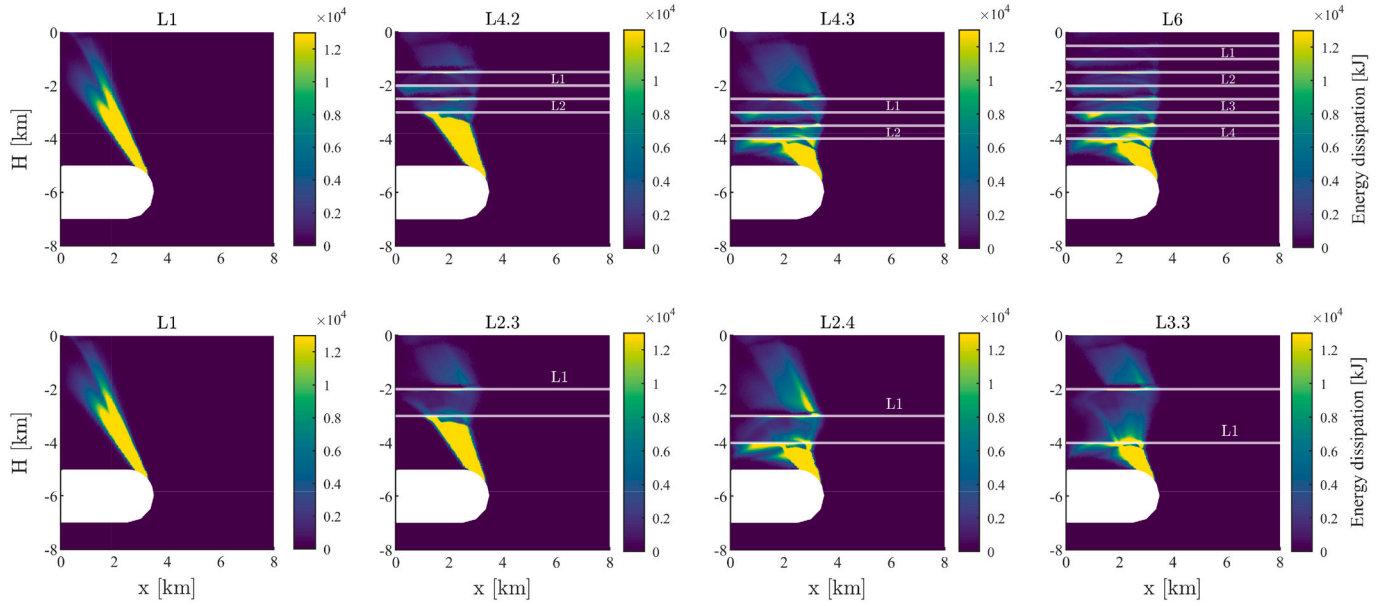

Fig. 9. Cross-section maps of distribution of shear energy dissipation (in kJ) in the overburden of the magma chamber in different simulations (for $R = 0.71$). In both upper and lower row, overburden in left simulation is homogeneous. Three other simulations in top row have multiple weak layers of thickness $t = \frac{1}{10}H$ (bounded by horizontal white lines) at variable depth. Tests L4.2 and L4.3 implement two weak layers, whereas Test L6 implements four weak layers. The three other simulations in bottom row have a single weak layer, (1) the thickness of which is the cumulative thickness of the thin weak layers of the corresponding simulation in the top row, and (2) the depth of which is the same as the depth of the deepest weak layer of the corresponding simulation in the top row.

3.4. *Effect of multiple layers*

All simulations presented above implement a single weak layer, whereas the Earth's crust is often made of multiple layers, such as lava flow piles and sedimentary strata. We thus implemented multiple layers in the simulations to test their effects on the onset of caldera collapse. In Fig. 9, the upper row displays the results from simulations with multiple thin weak layers (two in Tests L4.2 and L4.3; four in Test L6), of thickness $t = \frac{1}{10}H$. The simulations in the bottom row display simulations with a single weak layer, (1) the thickness of which is the cumulative thickness of the thin weak layers of the corresponding simulations in the top row, and (2) the depth of which is the same as the depth of the deepest weak layer of the corresponding simulations in the top row. Note that the left simulation in both top and bottom rows of Fig. 9 is the homogeneous model of Test L1 for reference.

In both Tests L4.2 and L2.3 (second column of Fig. 9), the depth of the deepest weak layer is $h = \frac{3}{5}H$, *i.e.* at intermediate depth in the models. In both simulations, the damage is concentrated and restricted below the bottom of the deepest weak layer, and very little difference is noticeable between models with single and multiple layers.

When the deepest weak layer is deeper (Tests L4.3, L2.4, L6 and L3.3), the effect of multiple layering is more prominent (Fig. 9). First, the amplitude of the damage at the surface of the models is lower above the multiple layers than above a single layer (compare Tests L4.3-L2.4 and Tests L6-L3.3; Fig. 9), suggesting that multiple layers constrain more the damage at depth. In addition, the distribution of the damage with multiple layers is more complex than with a single layer. In both one-layer-Tests L2.4 and L3.3, only a single horizontal damage band is

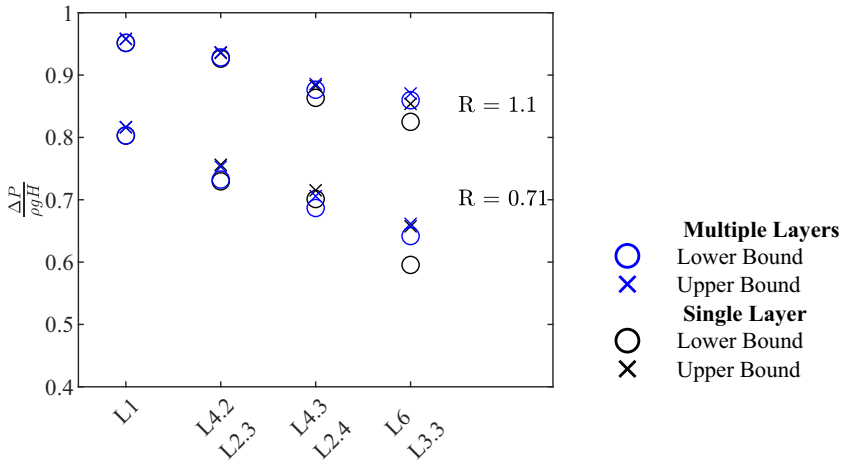

Fig. 10. Plot of the critical chamber underpressure relative to lithostatic pressure as a function of layer depth of multiple $\frac{1}{10}H$ thick weak layers (in blue) and a single layer, two tests with a $\frac{1}{5}H$ and one test with a $\frac{2}{5}H$ thick weak layer (in black). Circles gives the lower bound solution, while crosses give the upper bound solution.

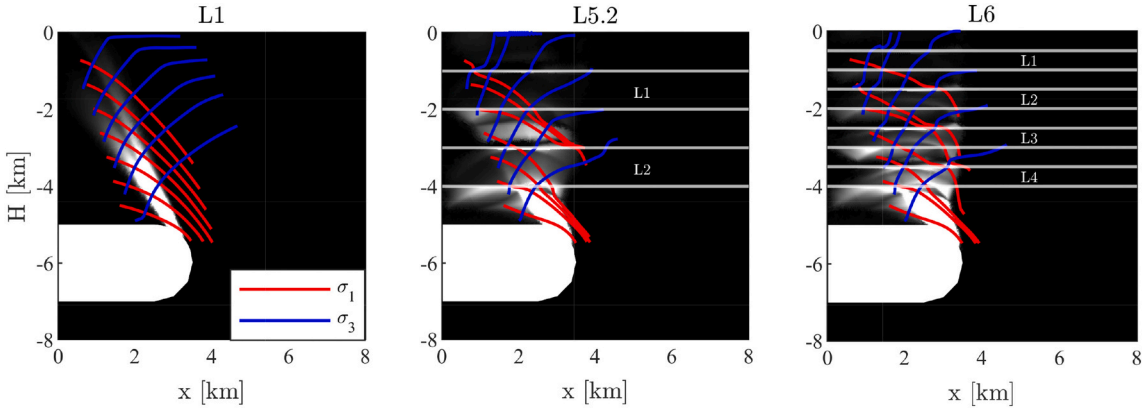

Fig. 11. Cross-section maps of stress trajectories (grey-level background) and plastic energy dissipation in Tests L1 (homogeneous overburden), L5.2 (two weak layers of thickness $\frac{1}{5}H$), and L6 (four weak layers of thickness $\frac{1}{10}H$) (for $R = 0.71$). σ_1 is in red and σ_2 in blue.

visible below the weak layer, whereas several horizontal damage bands are visible below the weak layers (and to a lower extent at the top of the weak layers) in two-layer-Tests L4.3 and L6. Finally, the damage pattern in Test L3.3 suggests that the main structures are sub-vertical or steeply-dipping when the weak layer is thick, whereas the expected structures are dominantly parallel to the weak layers when the layers are thin (Fig. 9, right column).

The overall kinematics of the damage are similar with multiple layers (Tests L4.3 and L6) and a single layer (L2.4 and L3.3) (Fig. 9). The damage zone nucleating at the edge of the magma reservoir below the deepest weak layer is outward dipping, with reverse kinematics, whereas within the weak layers the damage exhibits inward-dipping structures, with likely normal kinematics. Even though the damage near the surface of the models is very weak, the simulations suggest that the radius of the subsiding overburden is larger in models with multiple layers than with a single layer (Fig. 9).

Fig. 10 shows that the change in relative underpressure ($\Delta P/\rho gH$) needed to trigger failure is quite similar for models with multiple weak layers (blue) and models with a single weak layer (black). However, the gap between the lower bound and upper bound solution is increased for Test L6 and Test L3.3, indicating that the critical pressure at failure is less constrained for a larger amount of weak layers within the crust. This likely results from resolution limitations, as resolving many thin layers necessitates more elements than what we allow in our simulations.

3.5. Stress analysis

In addition to computing the distribution of damage and reservoir pressure at failure of the overburden, the OptumG2 software also computes stresses within the model. From the stress tensors, it is possible to calculate the trajectories of the principal stresses σ_1 and σ_3, which are represented by the red and blue curves, respectively, in Fig. 11. Fig. 11 displays three characteristic simulations, one homogeneous (Test L1, left), one with thick layers (Test L5.2, centre), and one with thin layers (Test L6, right).

In the homogeneous model Test L1 (Fig. 11, left), the trajectories of σ_1 and σ_3 exhibit gradual variations across the model, with no sudden change in slope and curvature. The σ_1 trajectories exhibit an angle of $\approx 30^\circ$ degrees with respect to the general orientation of the outward dipping damage zone; conversely, the σ_3 trajectories exhibit an angle of $\approx 60^\circ$ with the damage zone. Such configuration is compatible with (1) reverse kinematics of the damage zone and (2) the angle of internal friction ($\phi = 30^\circ$) of the host rock.

The stress trajectories in models with weak layers exhibit more complex patterns (Fig. 11, centre and right). The average slopes of the σ_1 trajectories in the damage zone are lower in the layered models than in the homogeneous Test L1. The average slopes of the σ_1 trajectories are lowest in the model with multiple thin weak layers. Thus, the presence of weak layers induce rotations of the principal stresses in the damage area. In addition, the slopes of the σ_1 trajectories exhibit sharp bends

across the layered models: the σ_1 trajectories become gently-dipping downward when crossing the top boundaries of the weak layers, and become steeper downward through the weak layer. The increasing complexity in the patterns of stress trajectories correlates with the increasing complexity of the distribution of the damage.

One can notice in Test L6 that the σ_1 trajectories at the outer edge of the damage area becomes steep (70°), at an angle of $\approx 30^\circ$ with the inward-dipping damage band segments between the weak layers (Fig. 11, right). This configuration is compatible with normal faulting, whereas the stress/damage zone configuration below the deepest weak layer is compatible with reverse faulting kinematics.

4. Interpretation

In all simulations, the intensity of the damage zone is highest near the chamber edge and fades towards the surface. This is especially prominent in the models with no layer (Fig. 3), but this pattern is also visible in the simulations with weak layers (Figs. 4, 5, 7, 9). This systematic result is in good agreement with our current understanding of caldera fault nucleation at the chamber edge when magma reservoir is under-pressured. (*e.g.,*Roche et al., 2000; Geyer et al., 2006; Holohan et al., 2015; Fontaine et al., 2019). In addition, the damage zones exhibit different characteristics for the different R-values (Fig. 3). For $R = 0.19$ the damage zone is curved outward (Fig. 3, left), while $R = 0.71$ and $R = 1.1$ have a straight damage zone (Fig. 3, centre and right). The damage zone also reaches the surface for $R = 0.19$ and $R = 0.71$ (Fig. 3, left and centre), while it does not in the simulation with $R = 1.1$ (Fig. 3, right). These results are in good agreement with existing models with varying values of R (*e.g.,*Roche et al., 2000; Geyer et al., 2006; Holohan et al., 2015).

The roof aspect ratio R also affects the relative underpressure at failure, both for simulations with and without layers. Fig. 6 shows that the underpressure at failure in Test L1 ($R = 0.19$) is around 25% of the confining pressure, while the underpressure at failure for $R = 0.71$ and $R = 1.1$ is $\approx 80\%$ and $\approx 95\%$, respectively, of the confining pressure. We infer that chambers with larger values of R require a significantly higher underpressure to trigger failure and collapse, and are hence more stable than chambers with smaller R, in agreement with the theoretical model of Roche and Druitt (2001). The consistency between our limit analysis models and former models validate the physical relevance of our approach. The following paragraphs build on this conclusion and provide our interpretations of the effects of weak layers on caldera collapse.

4.1. Effect of implementing weak layers

In the reference homogeneous Test L1, the damage zone is continuous and reaches the surface (Fig. 4, left), whereas the damage zone in the models with one weak layer is restricted under the layer and does not reach the surface (Figs. 4, 7, 9). The stress trajectory maps display local rotations of the principal stresses at the weak layers (Fig. 11, centre and right). These results suggest that weak layers inhibits the upward growth of caldera faults, and that weak layers might work as stress barriers.

The models implementing weak layers display more distributed damage than the localised damage zone in the homogeneous models (Figs. 4, 7, and 9). In addition, the local stress rotation within the weak layers is associated with the rotation of the damage zone from outward-dipping to inward-dipping (Fig. 5). Both geometries accommodate the downward displacement of the reservoir's overburden, therefore the outward-dipping segments exhibit reverse kinematics, whereas the inward-dipping segments exhibit normal kinematics. Our models thus suggest that weak layers distribute the damage during caldera collapse and lead to complex normal and reverse kinematics of the caldera fault. We infer that the weak layers act as local detachments that mechanically decouple the rock mass under and above them. These results also highlight that the assumption of straight ring faults is idealised.

In all the models with weak layers, regardless their depth and thickness, the required relative underpressure in the magma chamber to initiate failure is lower than in the homogeneous models (Figs. 6, 8, 10). This result is intuitive, as the overall strength of the reservoir's overburden is reduced. These results illustrate that failure is more likely to occur for a crust containing weak layers.

4.2. Effect of layer depth

Fig. 4 shows that the deeper a layer of thickness $\frac{1}{5}H$, the more distributed is the damage. In addition, layer-parallel damage below the weak layer becomes prominent when the layer is deeper. Similar effects are produced in models with different layer thickness (Fig. 7). We infer that the closer the layer is from the magma reservoir, the more effects it has on the damage distribution in the overburden. The deepening of the layers also reduces the critical relative pressure required for failure (Fig. 6). This trend is observed for all the R-values, however a bit weaker for $R = 0.19$. We interpret these results as a consequence of the caldera fault nucleation at the edge of the reservoir: the shorter the distance between the reservoir roof and the weak layer, the more interactions occur and the more the weak layer affects the distribution of damage.

4.3. Effect of layer thickness

Our models show that thick layers enhance the distribution of damage above the weak layer, compared to thinner layers (Fig. 7). This is more prominent for the models with deeper layers (Test L2.4 compared with L3.3, Fig. 7). We infer that the mechanical decoupling effect of a weak layer, as inferred in Section 4.1, is more prominent for thick weak layers than for thin weak layers.

The thickness of weak layers also affects the relative pressure required for failure ($\Delta P/\rho gH$) (Fig. 8). Thicker layers require lower values of $\Delta P/\rho gH$, which is intuitive as the overall strength of the overburden is lowered. This effect is more prominent when the thick layer is deeper. We infer that initial failure is more likely to occur if there are thick weak layers within the crust, preferentially located near the chamber.

4.4. Effect of multiple layers

The previous sections addressed the effects of a single weak layer on caldera fault morphology and on magma underpressure required for collapse. Nevertheless, the models implementing multiple layers show a more complex effect with respect to models with a single layer. The difference is visible by comparing Test L4.3 with L2.4, and Test L6 with L3.3 (Fig. 9); note that the summed thickness of the weak layers in these pairs of simulations are the same. These results show that the damage amplitude above the shallowest weak layer is reduced in models with multiple layers. Multiple weak layers also affect the distribution of damage, creating several layer-parallel damage bands in the overburden and distributing the damage over a broader zone. This damage spreading is in line with the more complex stress trajectories displayed in Fig. 11 (right column).

Fig. 10 shows that the values of $\Delta P/\rho gH$ are very similar in models with a single or with multiple layers, with the same total thickness of weak rocks. We infer that the distribution of the weak rocks in a single or multiple layers has limited effect on the onset of caldera collapse.

5. Discussion

5.1. Model validity and limitations

The results of the reference homogeneous tests in this study (Fig. 3) are in agreement with homogeneous models of caldera collapse in the literature. The caldera faults with $R = 0.71$ and $R = 1.1$ are similar to the initial caldera faults observed in laboratory studies (*e.g.,*Roche et al.,

2000; Acocella, 2007; Burchardt and Walter, 2010). The reservoir critical pressure at failure exhibits similar trends than in former studies, *i.e.,* lower *R*-values require lower critical pressure for initiating caldera collapse (Roche and Druitt, 2001). This consistency supports the physical relevance of limit analysis modelling for studying caldera collapse processes.

There are limitations with all modelling approaches, and the use of limit analysis is not an exception. The main limitation of using limit analysis is that it only provides information at the initial stage of failure, and cannot model the evolution of the collapse, and so the final caldera structure. The pressure within the magma chamber is also treated as a homogeneous pressure source, hence magma flow processes, volatile content and variation of properties throughout the chamber is not taken into account. The thermal effect of the magma chamber is also not taken into account, even though it might alter the rheology of the surrounding crust (Gregg et al., 2012). Our models neither do account for topography nor tectonic stress, whereas local topography affects the local stress field (*e.g.,*Walter and Troll, 2001; Lavallée et al., 2004; Kervyn et al., 2009) and tectonic stress can modify the geometry of caldera faults (*e.g.,*Holohan et al., 2005).

We are aware that the cohesion and friction angle values used in our models are very low and cannot account for intact rocks. Implementing such low values is indicative whether investigating the effects of weak layers are relevant or not: if negligible effect were observed in our models, it would indicate that weak layers are not relevant in understanding caldera collapse. Conversely, our results show that weak layers are relevant. The next step is to implement a parameter study to investigate which cohesion and friction angle values are more prone to affect caldera collapse.

Note that even though the cohesion and friction values are extremely low to account for intact rocks, processes at work at active volcanoes can considerably reduce rock strength: (1) rock alteration to clay (*e.g.,*Moore and Rymer, 2007; Carpenter et al., 2009; Giorgetti et al., 2015); (2) high fluid overpressures can considerably reduce effective stresses, which is equivalent to reducing rock cohesion and friction (*e.g.,*Mourgues and Cobbold, 2003) and can affect the deformation of volcanic edifices (*e.g.,* Reid et al., 2001; Merle and Lénat, 2003; Merle et al., 2010). These phenomena are common in geothermal systems at active volcanoes. All in all, the combination of weak rock lithology, alteration and high fluid pressures can lead to extremely low strength values likely similar to those implemented in our models.

5.2. The relevance of weak layers

The differences between the homogeneous tests and the layered tests in our study show that weak layers lead to stress rotations and distribution of damage over a broader area. Damage distribution causes local changes in the caldera fault geometry and kinematics, as the damage exhibits alternating inward and outward dipping segments (Figs. 4, 5 and 9). This damage pattern significantly deviates from the simple outward dipping bell-shaped faults obtained in homogeneous models (*e.g.,*Roche et al., 2000; Geyer et al., 2006; Burchardt and Walter, 2010; Liu et al., 2019), where the damage is localised along the initial fault, with a limited amount of damage affecting the surrounding crust. Given that the Earth's crust is layered in volcanic and sedimentary settings, our results show that layering likely plays a key role during caldera collapse in nature. This conclusion corroborates the models of tectonic deformation and magma emplacement (Rossi and Storti, 2003; van Gent et al., 2010; Abdelmalak et al., 2016), which also highlight the key role of layering in geological processes.

The difference in subsurface damage distribution with or without layers likely leads to different surface deformation prior to collapse at the surface. Homogeneous models predict that caldera subsidence is accommodated by a localized caldera fault (Figs. 10 and 9), the surface expression of which is an individual scarp (Fig. 12) (Roche et al., 2000; Acocella, 2007; Liu et al., 2019). Conversely, the subsurface damage distribution in models with weak layers likely results in distribution of the surface subsidence (see tectonic models of Holland et al., 2006; van Gent et al., 2010). We infer that subsurface layering might cause a wider subsidence area characterised by a downsag morphology prior to surface collapse (Fig. 12). This conclusion is supported by the numerical models of Holohan et al. (2017), which show how surface subsidence is affected by subsurface damage distribution prior to surface collapse.

5.3. Plastic versus elastic modelling

Fig. 11 evidences abrupt rotations of the principal stress trajectories when weak layers are implemented. In general, the principal stress trajectories are rotated within the weak layers and have an abrupt change at the contact between the weak layer and the host rock (Fig. 11). The complexity of the stress trajectories increases with increasing number of weak layers. Similar stress trajectories rotations have been documented in layered static elastic models of reservoir inflation (*e.g.,*Gudmundsson and Brenner, 2005; Gudmundsson and Philipp, 2006). In the elastic models, the stress rotations result from contrasts of Young's modulus between the layers, whereas in our models the stress rotations are due to contrasting cohesion and angle of friction. We infer that both elastic properties and the Coulomb properties of layered rocks can lead to prominent stress rotations. This result strongly suggests that stress analyses of geological systems also need to take into account variable Mohr–Coulomb properties of rock formations, not only their elastic properties.

Even though elastic models are able to predict stress rotation in layered or heterogeneous models (Gudmundsson and Brenner, 2005; Gudmundsson and Philipp, 2006; Long and Grosfils, 2009; Browning and Gudmundsson, 2015a), they are unable to calculate the variable location and kinematics of the damage as evidenced in our models. Limit analysis modelling thus offers great advantages with respect to static elastic models. We infer that the use of elastic modelling to simulate geological processes controlled by non-elastic brittle failure likely misses important aspects about the presence of a stress barrier and distributed inelastic damage. This highlights the importance of using a plastic (or elasto-plastic) modelling approach, instead of only elastic, as it provides a more realistic picture on the overall effect the weak layer has on the crust (Souche et al., 2019).

5.4. Easier to initiate, harder to propagate?

Our simulations show that the implementation of weak layers reduces the required underpressure needed to initiate failure (Fig. 6, 8 and 10). This indicates that failure is more likely to occur when weak layers are present within the crust, especially when they are located closer to the chamber and constitutes a larger part of the crust. This is expected, as the presence of weak layers lowers the overall strength of the crust (Byerlee, 1978; Jackson, 2002; Long and Grosfils, 2009). Due to this effect, the presence of weak layers within the crust might be of great importance, as it may have implications on hazard assessments if failure is initiated earlier than originally assumed. Conversely, even though the presence of weak layers might favour fault initiation, the layers also prevent the caldera fault from reaching the surface due to stress barriers, causing distributed damage and in some cases sub-horizontal damage bands (*e.g.,*Fig. 9). This style of faulting makes full caldera collapse less favourable.

5.5. Geological and geophysical implications

Our models suggest that the presence of weak layers enhances the formation of horizontal damage bands (Fig. 9), which can detach the rock masses above and below. Such internal decoupling mechanism and stress barriers due to weak layers are in agreement with the scenario observed at the 2007 caldera collapse of Piton de la Fournaise, Réunion Island (Fontaine et al., 2019). There, four subsurface precursory collapse

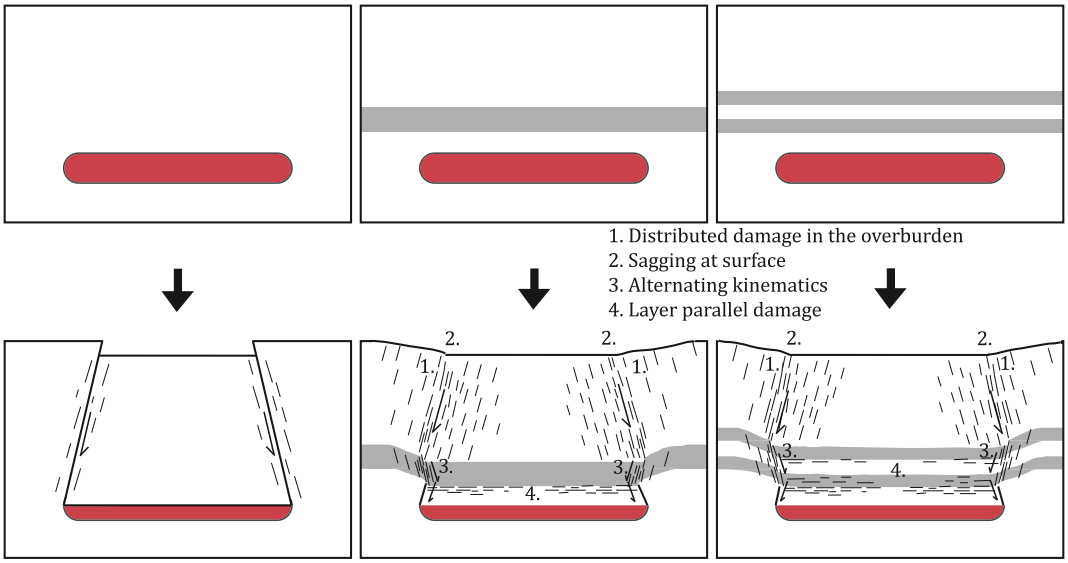

Fig. 12. Illustration of the main findings form this paper, highlighting the difference between simulating a caldera collapse with and without the presence of weak layers within the crust.

events were detected before the main collapse event at the surface. These precursory collapse events, without any surface rupture, have been inferred to result from downward motion of blocks of the rock column through a ring fault system. Our study suggests that weak layers (*e.g.,* tuff layers, scoria layers) promote the splitting of the rock column and episodic collapse events before collapse reaches the surface.

Our layered models evidence that weak layers enhance damage distribution, stress rotations and change in dip directions of damage zones, leading to alternating normal and reverse fault kinematics, and favours downsag subsidence morphology. This result is in agreement with the scenario of the 2014–2015 caldera development at Bárðarbunga volcano, Iceland (Riel et al., 2015; Gudmundsson et al., 2016; Rodríguez-Cardozo et al., 2021). Based on the profiles of the surface deformation, it was argued by Browning and Gudmundsson (2015b) that the event was related to distributed damage and subsidence rather than full caldera collapse. In addition, the seismicity was distributed, and the calculated focal mechanisms indicated both normal and reverse faulting (Rodríguez-Cardozo et al., 2021). The similarity between these observations and our results suggest that the layering of the crust might have affected, at least partly, the caldera mechanism at Bárðarbunga volcano.

6. Conclusion

This paper describes results of limit analysis numerical modelling to explore the effect of weak rock layers, *i.e.* low cohesion and low friction, on the onset of caldera collapse. We tested the effects of the position, thickness and number of the weak layers. The following points summarize the conclusions of our study.

- The presence of weak layers within the crust favours the onset of caldera collapse, as it reduces the critical magma underpressure within the magma chamber to initiate roof failure. This effect is more pronounced with greater cumulated thickness of weak layers.
- In homogeneous models, the onset of caldera collapse is accommodated by a simple, localized outward dipping reverse damage band (caldera fault), whereas in layered models caldera collapse is accommodated by more complex damage structures.
- Weak layers confine damage underneath the layers, limiting the growth of the caldera fault toward the surface. Calculated stress trajectories are rotated across weak layers, showing that weak layers act as stress barriers. The effect of weak layers is stronger when the layer is closer to the magma reservoir, where layer-parallel damage form underneath the layer, interpreted as a potential detachment level.
- Weak layers distribute the damage in the overburden, in comparison with the localized damage in homogeneous models. In addition, weak layers lead to local rotation of damage zone from outward-dipping to inward-dipping structures, triggering alternating reverse and normal kinematics, respectively, in the damage zone.
- Multiple layers enhance more distribution of the damage and several layer-parallel damage bands, *i.e.* several local detachment layers.
- The presence of weak layers makes the initiation of roof failure easier, but their stress barrier effect inhibits the faults from reaching the surface.
- The subsurface distribution of damage due to weak layers may lead to more distributed surface subsidence, enhancing sagging phase before a caldera fault reaches the surface.
- Finally, internal detachments due to weak layers are likely important for observed episodic transient subsurface collapse episodes before collapse occurs at surface.

All in all, our plastic models predict significant stress perturbations as a result of varying Mohr–Coulomb properties only. Our study thus shows that widely used static elastic models are not sufficient for physically relevant stress analyses of geological systems. In addition, our study shows that plastic (or elasto-plastic) models are necessary to predict location and extent of inelastic damage accommodating volcano deformation and failure.

Declaration of Competing Interest

The authors declare the following financial interests/personal relationships which may be considered as potential competing interests: Olivier Galland reports financial support and article publishing charges were provided by University of Oslo Department of Geosciences.

Data availability

Data will be made available on request.

Acknowledgement

The authors thank Optum Computational Engineering for giving free

access and use of software OptumG2 for academic purposes. We gratefully acknowledge the constructive reviews of Drs. Pauline Souloumiac and John Browning.

References

Abdelmalak, M.M., Bulois, C., Mourgues, R., Galland, O., Legland, J.B., Gruber, C., 2016. Description of new dry granular materials of variable cohesion and friction coefficient: implications for laboratory modeling of the brittle crust. Tectonophysics 684, 39–51.

Acocella, V., 2007. Understanding caldera structure and development: an overview of analogue models compared to natural calderas. Earth Sci. Rev. 85, 125–160.

Anderson, K.R., Johanson, I.A., Patrick, M.R., Gu, M., Segall, P., Poland, M.P., Montgomery-Brown, E.K., Miklius, A., 2019. Magma reservoir failure and the onset of caldera collapse at kīlauea volcano in 2018. Science 366, eaaz1822. https://doi.org/10.1126/science.aaz1822.

Bartley, J.M., Glazner, A.F., Mahan, K.H., 2012. Formation of pluton roofs, floors, and walls by crack opening at Split Mountain, Sierra Nevada, California. Geosphere 8, 1086–1103.

Browning, J., Gudmundsson, A., 2015a. Caldera faults capture and deflect inclined sheets: an alternative mechanism of ring dike formation. Bull. Volcanol. 77, 4.

Browning, J., Gudmundsson, A., 2015b. Surface displacements resulting from magma-chamber roof subsidence, with application to the 2014–2015 Bardarbunga–Holuhraun volcanotectonic episode in Iceland. J. Volcanol. Geoth. Res. 308, 82–98.

Burchardt, S., Tanner, D.C., Krumbholz, M., 2012. The slaufrudalur pluton, southeast iceland-an example of shallow magma emplacement by coupled cauldron subsidence and magmatic stoping. Geol. Soc. Am. Bull. 124, 213–227.

Burchardt, S., Walter, T.R., 2010. Propagation, linkage, and interaction of caldera ring-faults: comparison between analogue experiments and caldera collapse at Miyakejima, Japan, in 2000. Bull. Volcanol. 72, 297–308.

Byerlee, J., 1978. Friction of rocks. Pure Appl. Geophys. 116, 615–626.

Carpenter, B.M., Marone, C., Saffer, D.M., 2009. Frictional behavior of materials in the 3d safod volume. Geophys. Res. Lett. 36 https://doi.org/10.1029/2008GL036660.

Cole, J.W., Milner, D.M., Spinks, K.D., 2005. Calderas and caldera structures: a review. Earth Sci. Rev. 69, 1–26.

Cubas, N., Barnes, C., Maillot, B., 2013. Inverse method applied to a sand wedge: estimation of friction parameters and uncertainty analysis. J. Struct. Geol. 55, 101–113.

Davis, R.O., Selvadurai, A.P.S., 2005. Plasticity and Geomechanics. Cambridge University Press.

Druitt, T., Sparks, R., 1984. On the formation of calderas during ignimbrite eruptions. Nature 310, 679–681.

Fontaine, F.R., Roult, G., Hejrani, B., Michon, L., Ferrazzini, V., Barruol, G., Tkalčić, H., Di Muro, A., Peltier, A., Reymond, D., et al., 2019. Very-and ultra-long-period seismic signals prior to and during caldera formation on La Réunion Island. Sci. Rep. 9, 1–15.

van Gent, H., Holland, M., Urai, J., Loosveld, R., 2010. Evolution of fault zones in carbonates with mechanical stratigraphy - insights from scale models using layered cohesive powder. J. Struct. Geol. 32, 1375–1391.

Geshi, N., Shimano, T., Chiba, T., Nakada, S., 2002. Caldera collapse during the 2000 eruption of Miyakejima volcano, Japan. Bull. Volcanol. 64, 55–68.

Geyer, A., Folch, A., Martí, J., 2006. Relationship between caldera collapse and magma chamber withdrawal: an experimental approach. J. Volcanol. Geoth. Res. 157, 375–386.

Geyer, A., Marti, J., 2008. The new worldwide collapse caldera database (ccdb): a tool for studying and understanding caldera processes. J. Volcanol. Geoth. Res. 175, 334–354.

Giorgetti, C., Carpenter, B.M., Collettini, C., 2015. Frictional behavior of talc-calcite mixtures. J. Geophys. Res.: Solid Earth 120, 6614–6633. https://doi.org/10.1002/2015JB011970.

Gregg, P., De Silva, S., Grosfils, E., Parmigiani, J., 2012. Catastrophic caldera-forming eruptions: thermomechanics and implications for eruption triggering and maximum caldera dimensions on earth. J. Volcanol. Geoth. Res. 241–242, 1–12.

Gudmundsson, A., 2007. Conceptual and numerical models of ring-fault formation. J. Volcanol. Geoth. Res. 164, 142–160.

Gudmundsson, A., 2012. Magma chambers: formation, local stresses, excess pressures, and compartments. J. Volcanol. Geoth. Res. 237–238, 19–41.

Gudmundsson, A., 2020. Volcanotectonics: Understanding the Structure, Deformation and Dynamics of Volcanoes. Cambridge University Press, Cambridge.

Gudmundsson, A., Brenner, S.L., 2005. On the conditions of sheet injections and eruptions in stratovolcanoes. Bull. Volcanol. 67, 768–782.

Gudmundsson, A., Philipp, S.L., 2006. How local stress fields prevent volcanic eruptions. J. Volcanol. Geotherm. Res. 158, 257–268.

Gudmundsson, M., Jónsdóttir, K., Hooper, A., Holohan, E., Halldórsson, S., Ófeigsson, B., Cesca, S., Vogfjörd, K.S., Sigmundsson, F., Högnadóttir, T., Einarsson, P., Sigmarsson, O., Jarosch, A.H., Jónasson, K., Magnússon, E., Hreinsdóttir, S., Bagnardi, M., Parks, M.M., Hjörleifsdóttir, V., Pálsson, F., Walter, T.R., Schöpfer, M. P.J., Heimann, S., Reynolds, H.I., Dumont, S., Bali, E., Gudfinnsson, G.H., Dahm, T., Roberts, M.J., Hensch, M., Belart, J.M.C., Spaans, K., Jakobsson, S., Gudmundsson, G.B., Fridriksdóttir, H.M., Drouin, V., Dürig, T., Aðalgeirsdóttir, G., Riishuus, M.S., Pedersen, G.B.M., van Boeckel, T., Oddsson, B., Pfeffer, M.A., Barsotti, S., Bergsson, B., Donovan, A., Burton, M.R., Aiuppa, A., 2016. Gradual caldera collapse at Bárðarbunga volcano, Iceland, regulated by lateral magma outflow. Science 353, aaf8988. https://doi.org/10.1126/science.aaf8988.

Haug, Ø.T., Galland, O., Souloumiac, P., Souche, A., Guldstrand, F., Schmiedel, T., 2017. Inelastic damage as a mechanical precursor for the emplacement of saucer-shaped intrusions. Geology 45, 1099–1102. https://doi.org/10.1130/G39361.1.

Haug, Ø.T., Galland, O., Souloumiac, P., Souche, A., Guldstrand, F., Schmiedel, T., Maillot, B., 2018. Shear versus tensile failure mechanisms induced by sill intrusions: implications for emplacement of conical and saucer-shaped intrusions. J. Geophys. Res.: Solid Earth 123, 3430–3449.

Holland, M., Urai, J.L., Martel, S., 2006. The internal structure of fault zones in basaltic sequences. Earth Planet. Sci. Lett. 248, 301–315.

Holohan, E., Troll, V.R., Walter, T.R., Münn, S., McDonnell, S., Shipton, Z., 2005. Elliptical calderas in active tectonic settings: an experimental approach. J. Volcanol. Geoth. Res. 144, 119–136.

Holohan, E.P., Schöpfer, M.P.J., Walsh, J.J., 2015. Stress evolution during caldera collapse. Earth Planet. Sci. Lett. 421, 139–151.

Holohan, E.P., Sudhaus, H., Walter, T., Schöpfer, M., Walsh, J., 2017. Effects of host-rock fracturing on elastic-deformation source models of volcano deflation. Sci. Rep. 7, 10970.

Jackson, J.A., 2002. Strength of the continental lithosphere: time to abandon the jelly sandwich? GSA Today 12, 4–10.

Kavanagh, J.L., Pavier, M.J., 2014. Rock interface strength influences fluid-filled fracture propagation pathways in the crust. J. Struct. Geol. 63, 68–75.

Kennedy, B.M., Holohan, E.P., Stix, J., Gravley, D.M., Davidson, J.R.J., Cole, J.W., 2018. Magma plumbing beneath collapse caldera volcanic systems. Earth Sci. Rev. 177, 404–424.

Kervyn, M., Ernst, G.G.J., van Wyk de Vries, B., Mathieu, L., Jacobs, P., 2009. Volcano load control on dyke propagation and vent distribution: insights from analogue modeling. J. Geophys. Res. 114, B03401.

Krabbenhøft, K., Lyamin, A., Krabbenhøft, J., 2016a. Optumg2: Analysis. Optum Computational Engineering, Copenhagen, Denmark.

Krabbenhøft, K., Lyamin, A., Krabbenhøft, J., 2016b. Optumg2: Examples. Optum Computational Engineering, Copenhagen, Denmark.

Krabbenhøft, K., Lyamin, A.V., Hjiaj, M., Sloan, S.W., 2005. A new discontinuous upper bound limit analysis formulation. Int. J. Numer. Meth. Eng. 63, 1069–1088.

Lavallée, Y., Stix, J., Kennedy, B., Richer, M., Longpré, M.-A., 2004. Caldera subsidence in areas of variable topographic relief: results from analogue modeling. J. Volcanol. Geoth. Res. 129, 219–236.

Lipman, P., 1997. Subsidence of ash-flow calderas: relation to caldera size and magma-chamber geometry. Bull. Volcanol. 59, 198–218.

Liu, Y.K., Ruch, J., Vasyura-Bathke, H., Jónsson, S., 2019. Influence of ring faulting in localizing surface deformation at subsiding calderas. Earth Planet. Sci. Lett. 526, 115784.

Long, S.M., Grosfils, E.B., 2009. Modeling the effect of layered volcanic material on magma reservoir failure and associated deformation, with application to Long Valley caldera, California. J. Volcanol. Geoth. Res. 186, 349–360.

Martí, J., Geyer, A., Folch, A., Gottsmann, J., 2008. Chapter 6 a review on collapse caldera modelling. In: Gottsmann, J., Martí, Joan (Eds.), Developments in Volcanology, vol. 10. Elsevier, pp. 233–283.

Merle, O., Barde-Cabusson, S., van Wyk de Vries, B., 2010. Hydrothermal calderas. Bull. Volcanol. 72, 131–147.

Merle, O., Lénat, J.-F., 2003. Hybrid collapse mechanism at Piton de la Fournaise volcano, Reunion Island, Indian Ocean. J. Geophys. Res.: Solid Earth 108. https://doi.org/10.1029/2002JB002014.

Moore, D.E., Rymer, M.J., 2007. Talc-bearing serpentinite and the creeping section of the san andreas fault. Nature 448, 795–797.

Mourgues, R., Cobbold, P., 2003. Some tectonic consequences of fluid overpressures and seepage forces as demonstrated by sandbox modelling. Tectonophysics 376, 75–97.

Reid, M.E., Sisson, T.W., Brien, D.L., 2001. Volcano collapse promoted by hydrothermal alteration and edifice shape, Mount Rainier, Washington. Geology 29, 779–782.

Reynolds, P., Holford, S., Schofield, N., Ross, A., 2018. The importance of subsurface lithology in controlling magma storage v. eruption: an example from offshore southern Australia. J. Geol. Soc. 175, 694.

Riel, B., Milillo, P., Simons, M., Lundgren, P., Kanamori, H., Samsonov, S., 2015. The collapse of Bárðarbunga caldera, Iceland. Geophys. J. Int. 202, 446–453.

Roche, O., Druitt, T.H., 2001. Onset of caldera collapse during ignimbrite eruptions. Earth Planet. Sci. Lett. 191, 191–202.

Roche, O., Druitt, T.H., Merle, O., 2000. Experimental study of caldera formation. J. Geophys. Res.: Solid Earth 105, 395–416.

Rodríguez-Cardozo, F., Hjörleifsdóttir, V., Jónsdóttir, K., Iglesias, A., Franco, S.I., Geirsson, H., Trujillo-Castrillón, N., Hensch, M., 2021. The 2014–2015 complex collapse of the Bárðarbunga caldera, Iceland, revealed by seismic moment tensors. J. Volcanol. Geoth. Res. 416, 107275.

Rossi, D., Storti, F., 2003. New artificial granular materials for analogue laboratory experiments: aluminium and siliceous microspheres. J. Struct. Geol. 25, 1893–1899.

Schmiedel, T., Galland, O., Haug, Ø.T., Dumazer, G., Breitkreuz, C., 2019. Coulomb failure of earth's brittle crust controls growth, emplacement and shapes of igneous sills, saucer-shaped sills and laccoliths. Earth Planet. Sci. Lett. 510, 161–172.

Souche, A., Galland, O., Haug, Ø.T., Dabrowski, M., 2019. Impact of host rock heterogeneity on failure around pressurized conduits: Implications for finger-shaped magmatic intrusions. Tectonophysics 765, 52–63.

Souloumiac, P., Krabbenhøft, K., Leroy, Y.M., Maillot, B., 2010. Failure in accretionary wedges with the maximum strength theorem: numerical algorithm and 2d validation. Comput. Geosci. 14, 793–811.

Thomson, K., Schofield, N., 2008. Lithological and structural controls on the emplacement and morphology of sills in sedimentary basins. Geol. Soc. Lond. Spec. Publ. 302, 31–44.

Walter, T.R., Troll, V.R., 2001. Formation of caldera periphery faults: an experimental study. Bull. Volcanol. 63, 191–203.

Yao, Z., He, G., Li, C.-F., Dong, C., 2018. Sill geometry and emplacement controlled by a major disconformity in the Tarim Basin, China. Earth Planet. Sci. Lett. 501, 37–45.